Coherent feedback control of a single qubit in diamond

Coherent feedback control of a single qubit in diamond

Masashi Hirose[1] and Paola Cappellaro[1]

[1] *Research Laboratory of Electronics and Department of Nuclear Science and Engineering, Massachusetts Institute of Technology, Cambridge, Massachusetts 02139, USA*

Engineering desired operations on qubits subjected to the deleterious effects of their environment is a critical task in quantum information processing, quantum simulation and sensing. The most common approach is to rely on open-loop quantum control techniques, including optimal control algorithms, based on analytical [1] or numerical [2] solutions, Lyapunov design [3] and Hamiltonian engineering [4]. An alternative strategy, inspired by the success of classical control, is feedback control [5]. Because of the complications introduced by quantum measurement [6], closed-loop control is less pervasive in the quantum settings and, with exceptions [7, 8], its experimental implementations have been mainly limited to quantum optics experiments. Here we implement a feedback control algorithm with a solid-state spin qubit system associated with the Nitrogen Vacancy (NV) centre in diamond, using coherent feedback [9] to overcome limitations of measurement-based feedback, and show that it can protect the qubit against intrinsic dephasing noise for milliseconds.

In coherent feedback, the quantum system is connected to an auxiliary quantum controller (ancilla) that acquires information about the system's output state (by an entangling operation) and performs an appropriate feedback action (by a conditional gate). In contrast to open-loop dynamical decoupling (DD) techniques [10], feedback control can protect the qubit even against Markovian noise and for an arbitrary period of time (limited only by the ancilla coherence time), while allowing gate operations. It is thus more closely related to Quantum Error Correction schemes [11–14], which however require larger and increasing qubit overheads. Increasing the number of fresh ancillas allows protection even beyond their coherence time.

We can further evaluate the robustness of the feedback protocol, which could be applied to quantum computation and sensing, by exploring an interesting tradeoff between information gain and decoherence protection, as measurement of the ancilla-qubit correlation after the feedback algorithm voids the protection, even if the rest of the dynamics is unchanged.

To demonstrate coherent feedback with spin qubits, we choose two of the most common tasks for qubits, implementing the no-operation (NOOP) and NOT gates, while cancelling the effects of noise. A simple, measurement-based feedback scheme, exploiting one ancillary qubit, was proposed in [16]. The correction protocol (Fig. 1a) works by entangling the qubit-ancilla system before the desired gate operation. By selecting an entangling operation U_c appropriate for the type of bath acting on the system, information about the noise action is encoded in the ancilla state. After undoing the entangling operation, the qubit coherence can be restored by a feedback action,

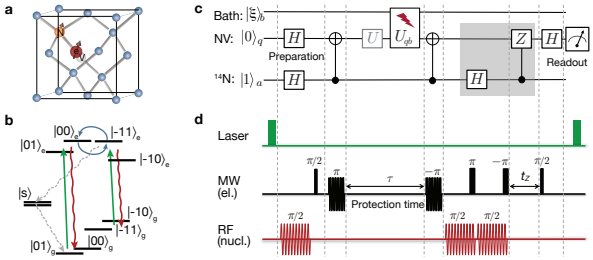

FIG. 1. **Feedback algorithm and experimental implementation**. **(a)** NV centre in diamond and **(b)** relevant energy levels of the spin system, showing polarisation processes under optical illumination [15]. **(c)** *Quantum circuit.* Hadamard gates prepare and read out a superposition state of the qubit, $|\phi\rangle_q = \frac{1}{\sqrt{2}}(|0\rangle + |1\rangle)$. Amid entangling gates between qubit and ancilla, the qubit is subjected to noise (and possibly unitary gates U). We assume the ancilla is not affected by the bath, yielding $\mathbb{1}_a \otimes U_{qb}(\tau)$, with $U_{qb}(\tau)$ the qubit-bath joint evolution. Given a dephasing bath, we set the entangling gate to $U_c = \sigma_x$ (conditional-NOT gate). More generally, upon undoing the entangling operation, the system is left in the state $|\Psi(\tau)\rangle = \frac{1}{\sqrt{2}}(|0\rangle_a K^+ |\phi_q, \xi_b\rangle + |1\rangle_a K^- |\phi_q, \xi_b\rangle)$, with $K^\pm = U_{qb} \pm U_c U_{qb} U_c^\dagger$. The entangling gate U_c is designed such that $K^+ = \mathbb{1}_q \otimes \chi_b^+$ and $K^- = U_q^\dagger \otimes \chi_b^-$, where $\chi_b^\pm$ act on the bath only, and U_q on the qubit. After measuring the ancilla, we could use a feedback operation U_q to restore the correct qubit state. The ancilla measurement is replaced by coherent feedback (shaded region) obtained by a controlled-correction gate (here $U_q = \sigma_z$ for dephasing noise). The final state of the combined system is then $\frac{1}{\sqrt{2}}(|0\rangle_a \chi_b^+ + |1\rangle_a \chi_b^-) |\phi\rangle_q |\xi\rangle_b$, which reveals how the qubit is now decoupled from the bath.
(d) *Experimental implementation.* The laser excitation polarises both spins. Black sinusoidal lines refer to selective MW pulses acting only in the $m_I = 1$ manifold (thus mimicking controlled-NOT gates), while solid bars indicate nonselective pulses. The RF excitation describes selective pulses in the $m_s = 0$ manifold. We use $\pi/2$ rotations about x to approximate Hadamard gates. To implement a nonselective RF $\pi/2$ gate on the nuclear spin we embed a nonselective MW π pulse into two consecutive RF $\pi/2$ pulses. The controlled-correction gate is implemented by free evolution (t_Z) under hyperfine coupling.

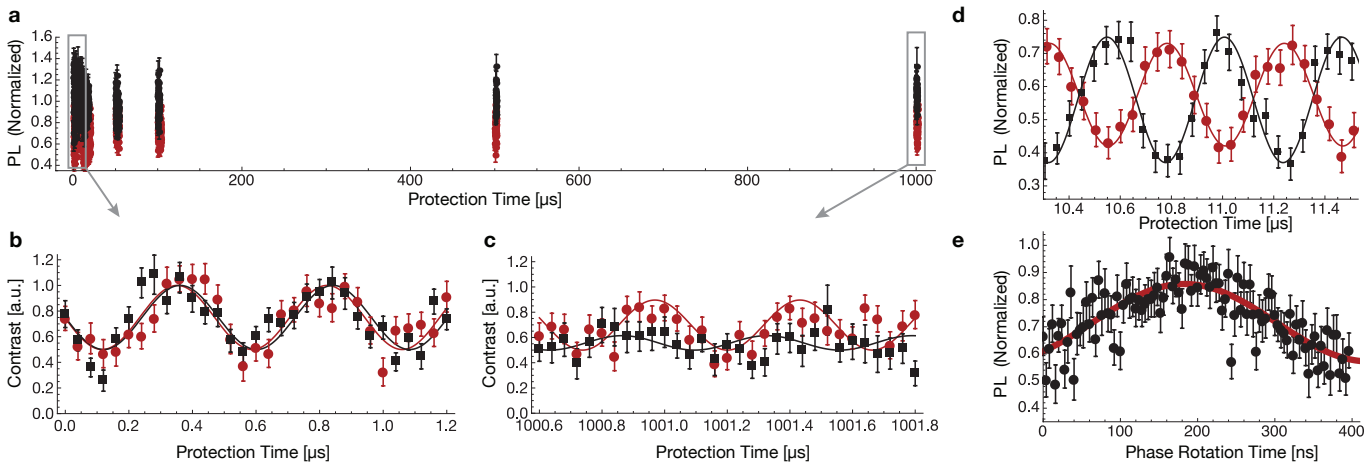

FIG. 2. **Experimental demonstration of the feedback-based protection algorithm**. **(a)** The signal –normalised Photoluminescence (PL) intensity– oscillates at the hyperfine coupling frequency, $A = -2.15$ MHz. The initial coherent superposition state of the qubit is preserved for a time $\tau > 1$ ms at 390 G (red dots), while we observe a sharp decrease in the signal amplitude at 514 G (black squares), where correlations between the qubit and ancilla states are partly measured. This is evident in the lower panels, where we compare the fidelity at short **(b)**, and long **(c)** times, for B =390 G and 514 G. To highlight the differences while taking into account different PL intensities at the two fields, we normalised all the data so that at short times the signal has the same (maximum) contrast. **(d)** Protected NOT gate (red circles). Here we show that the coherence of the qubit is protected for a time longer than the dephasing time, $\tau > T_{2e}^{\star}$, even when a NOT gate is applied. We compare the dynamics to the NOOP dynamics (black squares), clearly showing that the NOT gate inverts the state of the qubit, as signalled by the out-of-phase oscillations. **(e)** Weak measurement of the ancilla: normalised PL signal after a protection time $\tau = 8\mu$s, as a function of the ancilla measurement strength. In the experiment, we vary the ancilla measurement strength by changing the angle of the last controlled phase rotation gate. Error bars of all experimental data in the panels represent the signal standard deviation, calculated by error propagation from the PL intensity of the signal and of reference PL curves acquired for each data point for $m_s = \{0, -1\}$.

that is, measuring the ancilla and applying a correction operation U_q on the qubit, based on the measurement result. While this scheme applies to a broad class of environments, in the case of dephasing noise Ref. [16] proved the existence of the appropriate unitaries, $U_c = \sigma_x$ and $U_q = \sigma_z$. The principle of deferred measurements [17] allows postponing measurements until the end of a quantum algorithm. Here it enables replacing the ancilla measurement and classical feedback by coherent conditional gates. The final qubit state is then completely decoupled from the bath effects, which are instead imposed on the ancilla. Since the scheme is compatible with any gate that commutes with U_c, it is more flexible than DD techniques. Another advantage over DD techniques is that the scheme is valid independently of the characteristic time scale of the bath and thus it can be used even in the presence of a Markovian bath where DD fails. These two advantages enable using the feedback scheme for sensing, e.g., to detect transverse magnetic fields or, by a simple modification of the algorithm, to protect the sensing qubit from bit-flip errors while detecting fields aligned with the z quantisation axis [18–20].

We demonstrated experimentally this feedback-based protection algorithm with a spin system associated with a single Nitrogen Vacancy (NV) centre in diamond. This system has emerged as a good candidate for quantum information processing, as its electronic spin-1 can be optically polarised and measured, and presents long coherence times even at room temperature. Here we use an auxiliary qubit associated with the NV's ^{14}N nuclear spin-1, to protect the coherence of the NV electronic spin against dephasing noise. The Hamiltonian of the electronic-nuclear spin system is given by

$$\mathcal{H} = \Delta S_z^2 + \omega_e S_z + Q I_z^2 + \omega_n I_z + A S_z I_z + B(S_x I_x + S_y I_y),$$

where S and I are the electron and nuclear spin operator respectively, $\Delta = 2.87$ GHz is the electronic zero-field splitting and $Q = -4.95$ MHz the nuclear quadrupolar interaction. The two spins are coupled by an isotropic hyperfine interaction with $A = -2.16$ MHz and a transverse component $B = -2.62$ MHz [21] that can be neglected to first order. A magnetic field is applied along the NV crystal axis [111] to lift the degeneracy of the $m_s = \pm 1$ level, yielding the electron and nuclear Zeeman frequencies ω_e and ω_n. In the experiment we only use a subspace of the total system representing a two-qubit system. For convenience, we choose the space spanned by the four levels $\{|m_s, m_I\rangle = |0,1\rangle, |0,0\rangle, |-1,1\rangle, |-1,0\rangle\}$. The effective Hamiltonian can then be rewritten by using spin-1/2 operators and simplified by transforming to a rotating frame at the resonant frequency of the qubit $(\Delta - \omega_e)$ and the ancilla $(\omega_n + Q)$: $\mathcal{H}' = \frac{A}{4}(-\sigma_z^e + \sigma_z^n - \sigma_z^e \sigma_z^n)$.

In our high-purity diamond sample, decoherence processes of the electronic spin can be mainly attributed to

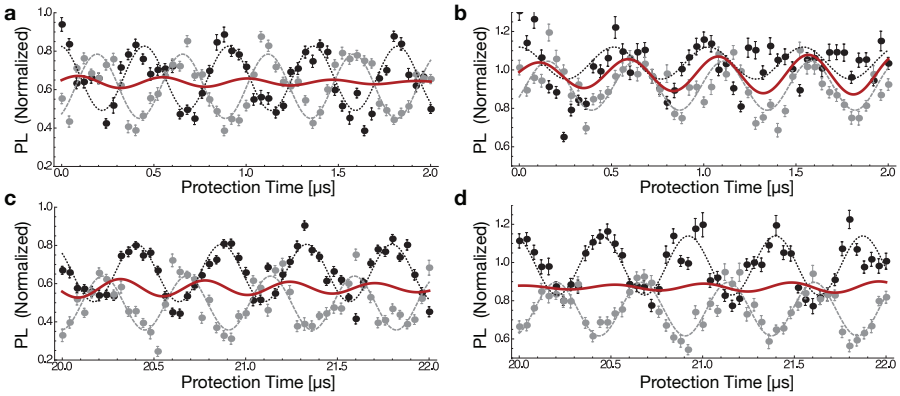

FIG. 3. **Partial measurement of the ancilla.** Comparison of the fidelity signal with (grey) and without (black) a π-pulse on the qubit, revealing the amount of information acquired about the ancilla qubit state. (**a, b**) show signals measured at short protection time, $\tau < T_{2e}^{\star}$ $(0-2\mu s)$, while (**c, d**) at longer times, $\tau > T_{2e}^{\star}$ $(20-22\mu s)$. Error bars are the signal standard deviation (see Fig. 2.) The data is fitted (solid lines) with the model described in Methods. At the lower magnetic field ($B = 390$G, (**a, c**)), the average of signals (red lines, obtained from the data fits) presents only weak oscillations, indicating that at this field the measurement only carry very little information about the ancilla state. For magnetic field close to the level anti-crossing ($B = 514$G, (**b, d**)), the oscillation of the average signal is more pronounced and can be observed until $\tau < T_{2e}^{\star}$ while it disappears at longer times. This is an indication that the ancillary spin effectively decoheres on the $T_{2e}^{\star}$ scale as a result of the feedback algorithm .

a bath of spin-1/2 ^{13}C nuclei in the lattice (1.1% natural abundance), yielding a short dephasing time $T_{2e}^{\star} \sim 4\mu s$. We can neglect the interaction between the bath and the ancillary spin, which couples very weakly to any source of magnetic field noise; indeed the much longer coherence time of the ^{14}N spin, $T_{2n}^{\star} \approx 3$ ms, is limited by the NV electronic spin relaxation and not by the ^{13}C bath.

In the experiment, the electronic spin qubit is initialised into the $m_s = 0$ state by optical excitation at 532 nm. At the chosen magnetic field strengths (390G-510G), optical pumping also polarises the nuclear spin into the $m_I = +1$ state, thanks to resonant polarisation exchange with the electronic spin in the excited state [15]. After initialising the qubit in the superposition state $|\phi\rangle_q = (|0\rangle_e + |1\rangle_e)/\sqrt{2}$, we implement the feedback-based protection algorithm using the control operations shown in Fig. (1b). Gate operations on the qubit and ancillary spins are performed by external microwave (MW) and radio frequency (RF) fields [22], respectively (see Methods). Because the noise is dephasing in nature, the feedback-based protection algorithm requires the entangling gate to be a controlled-NOT gate, $U_c = \sigma_x$, while the coherent feedback gate is implemented by a controlled Pauli-Z gate, $U_q = \sigma_z$ (see Fig. 1a and Methods). Finally, the qubit state can be optically read out by monitoring spin-state dependent fluorescence.

We measure the fidelity of the NOOP and NOT gates while varying the protection time τ. As shown in Fig. 2a, the feedback algorithm protects the qubit coherence against the noise created by the ^{13}C nuclear spin bath for times $\tau > 1$ ms, much longer than the dephasing time. While the spin-bath in this experimental system is non-Markovian and thus DD techniques have reached similar protection times [23], unlike DD this method would also be effective in the Markovian noise regime, with its ultimate limit set only by the coherence time of the ancillary spin and the qubit relaxation. These limits could be overcome by re-initialising the ancilla or, if additional ancillas (such as nearby ^{13}C spins) are available, by repeating the algorithm with fresh ancillas, or by concatenating layers of protections against multi-axis noise (see Methods). Moreover, our scheme is more flexible than other protection schemes, including coherent transfer to the ancilla qubit [24], as it still allows applying some gate operations on the qubit [16]. For example, in our implementation the qubit was still evolving under the action of the hyperfine coupling, as indicated by the coherent oscillations of the fidelity (these oscillations could be removed e.g. by an adequate timing choice). In addition, we can for example implement a NOT gate on the qubit during the feedback-protection algorithm (Fig. 2d), without degrading the protection, even at times much longer than the gate itself and independent of the time at which the gate is performed (see Methods).

The success of the feedback-based protection algorithm rests on the fact that the increased qubit entropy, due to the coupling to the environment, is dumped on the ancilla. This could be revealed by measuring the state of the ancilla, which would yield information about the noise, while preserving the qubit state. If instead information about the ancilla is collected by a correlated qubit-ancilla measurement, the protection fails [25], as it would happen in a measurement-based feedback for an imperfect ancilla readout. Here, we investigate this tradeoff between the protection power and information gain on the ancilla in two different experiments. First, we transfer a part of the ancilla entropy back to the qubit by employing a conditional gate that maps the state of the an-

cilla onto the qubit, correlating the two qubit states. By changing the angle of rotation of the conditional gate we can vary the strength of the ancilla measurement, from a weak measurement to a strong one. As more information about the ancilla is acquired, the fidelity of the protection gate decreases (Fig. 2b). Note that we can combine the conditional gate performing the weak measurement of the ancilla state with the last conditional Z-gate of the algorithm, thus in practice performing a conditional phase-shift gate. The qubit fidelity is maximised when the conditional gate performs the required π-rotation on the qubit, whereas it decreases when a different phase rotation is employed.

While this experiment clearly shows that the effectiveness of the protection is lost when a measurement of the ancilla-qubit correlation is performed, we can show that similar results also arise naturally from non-ideal experimental measurement conditions. We thus repeated the experiment at a different magnetic field, where our signal, the fluorescence intensity, carries information about the state of both the qubit and the ancilla, and their correlation. While at low magnetic field we can approximate the normalised measurement operator by $\overline{M}_0 = |0\rangle\langle 0| \otimes \mathbb{1}$, for magnetic fields close to the excited-state level anti-crossing ($B \approx 500$G, such that Zeeman energy $\omega_e = \gamma_e B$ is close to the excited-state zero-field splitting, $\Delta_e \approx 1.4$GHz) the normalised observable is $\overline{M}_0 - (\epsilon\,|10\rangle\langle 10| + \eta\,|00\rangle\langle 00|)$, where ϵ and η take into account that each electronic-nuclear spin level considered has a different fluorescence emission intensity due to the excited state dynamics [26].

Because at this magnetic field the measurement observable contains partial information about correlations between the qubit and ancilla states, the qubit fidelity at long times is reduced (Fig. 2a), reflecting the effects of the noise acting on the qubit. We thus reveal a trade-off between the amount of information acquired about the ancillary system and the protection that it provides to the qubit. In addition, we can single out a measurement of the ancilla alone, without qubit-ancilla correlations, by comparing the signal acquired so far with the signal after the qubit is rotated by a π pulse just prior to detection. If the measurements were independent of the state of the ancilla, the average of the two experiments should not vary in time (since it corresponds to measuring the identity operator). Indeed, this is what is observed in experiments performed at the lower magnetic field (Fig.3a, 3c); for a magnetic field close to the level anti-crossing, instead, oscillations indicate that we can extract information about the ancilla. However, at times longer than the qubit dephasing time, the state of ancilla has completely decohered (Fig. 3b, 3d), thus quenching these oscillations.

In conclusion, we performed coherent feedback control on a single solid-state qubit associated with the NV centre in diamond. The feedback algorithm was applied to protect the qubit coherence, while performing two essential qubit gates, NOOP and NOT gates, during the protection time. We showed that this feedback-based protection algorithm can protect the qubit coherence far beyond the dephasing time of the qubit, even if no active control is applied to decouple it from the noise. The algorithm can be extended to applications in quantum information processing and quantum sensing, and it could be implemented in many other hybrid spin systems, such as phosphorus [27] or antimony [28] donors in silicon, defects in silicon carbide [29] or quantum dots [30]. As we applied a coherent feedback protocol, thus avoiding measuring the state of the ancilla, the decoherent effects of the bath are effectively stored in the ancilla. We were thus able to explore an interesting compromise between the amount of information gained about the ancilla and the effectiveness of the protection algorithm. These results contribute towards elucidating the robustness of feedback control and paving the way for a more widespread adoption of close-loop control strategies for solid-state qubit systems.

Acknowledgements – We thank L. Viola, F. Ticozzi, M. Lukin and F. Jelezko for discussions. This work was supported in part by the U.S. Air Force Office of Scientific Research grant No. FA9550-12-1-0292 and by the U.S. Office of Naval Research grant No. N00014-14-1-0804.

[1] U. Boscain and P. Mason, J. Math. Phys. **47**, 062101 (2006).
[2] N. Khaneja, T. Reiss, C. Kehlet, T. Schulte-Herbuggen, and S. Glaser, J. Mag. Res. **172**, 296 (2005).
[3] X. Wang and S. Schirmer, Automatic Control, IEEE Transactions on **55**, 2259 (2010).
[4] A. Ajoy and P. Cappellaro, Phys. Rev. Lett. **110**, 220503 (2013).
[5] H. M. Wiseman and G. J. Milburn, Phys. Rev. Lett. **70**, 548 (1993).
[6] A. C. Doherty, K. Jacobs, and G. Jungman, Phys. Rev. A **63**, 062306 (2001).
[7] R. Vijay, C. Macklin, D. H. Slichter, S. J. Weber, K. W. Murch, R. Naik, A. N. Korotkov, and I. Siddiqi, Nature **490**, 77 (2012).
[8] C. Sayrin, I. Dotsenko, X. Zhou, B. Peaudecerf, T. Rybarczyk, S. Gleyzes, P. Rouchon, M. Mirrahimi, H. Amini, M. Brune, J.-M. Raimond, and S. Haroche, Nature **477**, 73 (2011).
[9] S. Lloyd, Phys. Rev. A **62**, 022108 (2000).
[10] L. Viola, E. Knill, and S. Lloyd, Phys. Rev. Lett. **82**, 2417 (1999).
[11] P. W. Shor, in *37th Annual Symposium on Foundations of Computer Science* (IEEE Comput. Soc. Press, Los Alamitos, CA, 1996) pp. 56–65.
[12] H. Taminiau, J. Cramer, T. van der Sar, V. Dobrovitski, and R. Hanson, Nat Nano **9**, 171 (2014).
[13] G. Waldherr, Y. Wang, S. Zaiser, M. Jamali, T. Schulte-Herbruggen, H. Abe, T. Ohshima, J. Isoya, J. F. Du, P. Neumann, and J. Wrachtrup, Nature **506**, 204 (2014).

[14] J. Cramer, N. Kalb, M. A. Rol, B. Hensen, M. S. Blok, M. Markham, D. J. Twitchen, R. Hanson, and T. H. Taminiau, arXiv:1508.01388 (2015).
[15] V. Jacques, P. Neumann, J. Beck, M. Markham, D. Twitchen, J. Meijer, F. Kaiser, G. Balasubramanian, F. Jelezko, and J. Wrachtrup, Phys. Rev. Lett. **102**, 057403 (2009).
[16] F. Ticozzi and L. Viola, Phys. Rev. A **74**, 052328 (2006).
[17] R. Griffiths and C.-S. Niu, Phys. Rev. Lett. **76**, 3228 (1996).
[18] E. M. Kessler, I. Lovchinsky, A. O. Sushkov, and M. D. Lukin, Phys. Rev. Lett. **112**, 150802 (2014).
[19] G. Arrad, Y. Vinkler, D. Aharonov, and A. Retzker, Phys. Rev. Lett. **112**, 150801 (2014).
[20] T. Unden, P. Balasubramanian, D. Louzon, Y. Vinkler, M. Plenio, M. Markham, D. Twitchen, I. Lovchinsky, A. Sushkov, M. Lukin, A. Retzker, B. Naydenov, L. McGuinness, and F. Jelezko, "Quantum metrology enhanced by repetitive quantum error correction," (2015), manuscript submitted for publication.
[21] M. Chen, M. Hirose, and P. Cappellaro, Phys. Rev. B **92**, 020101 (2015).
[22] A. Laraoui, F. Dolde, C. Burk, F. Reinhard, J. Wrachtrup, and C. A. Meriles, Nat. Commun. **4**, 1651 (2013).
[23] C. A. Ryan, J. S. Hodges, and D. G. Cory, Phys. Rev. Lett. **105**, 200402 (2010).
[24] J. J. L. Morton, A. M. Tyryshkin, R. M. Brown, S. Shankar, B. W. Lovett, A. Ardavan, T. Schenkel, E. E. Haller, J. W. Ager, and S. A. Lyon, Nature **455**, 1085 (2008).
[25] Y.-H. Kim, R. Yu, S. P. Kulik, Y. Shih, and M. O. Scully, Phys. Rev. Lett. **84**, 1 (2000).
[26] M. Steiner, P. Neumann, J. Beck, F. Jelezko, and J. Wrachtrup, Phys. Rev. B **81**, 035205 (2010).
[27] J. J. Pla, K. Y. Tan, J. P. Dehollain, W. H. Lim, J. J. L. Morton, F. A. Zwanenburg, D. N. Jamieson, A. S. Dzurak, and A. Morello, Nature **496**, 334 (2013).
[28] G. Wolfowicz, M. Urdampilleta, M. L. Thewalt, H. Riemann, N. V. Abrosimov, P. Becker, H.-J. Pohl, and J. J. Morton, Phys. Rev. Lett. **113**, 157601 (2014).
[29] M. Widmann, S.-Y. Lee, T. Rendler, N. T. Son, H. Fedder, S. Paik, L.-P. Yang, N. Zhao, S. Yang, I. Booker, A. Denisenko, M. Jamali, S. A. Momenzadeh, I. Gerhardt, T. Ohshima, A. Gali, E. Janzén, and J. Wrachtrup, Nature Mat. **14**, 164 (2015).
[30] E. A. Chekhovich, M. N. Makhonin, A. I. Tartakovskii, A. Yacoby, H. Bluhm, K. C. Nowack, and L. M. K. Vandersypen, Nature Mat. **12**, 494 (2013).
[31] G. Lindblad, Communications in Mathematical Physics **48**, 119 (1976).
[32] F. Bloch, Phys. Rev. **105**, 1206 (1957).
[33] M. Kälin and A. Schweiger, J. Chem. Phys. **115**, 10863 (2001).
[34] W. B. Mims, Phys. Rev. B **5**, 2409 (1972).
[35] P. Neumann, R. Kolesov, V. Jacques, J. Beck, J. Tisler, A. Batalov, L. Rogers, N. B. Manson, G. Balasubramanian, F. Jelezko, and J. Wrachtrup, New J. Phys. **11**, 013017 (2009).
[36] C. A. Meriles, L. Jiang, G. Goldstein, J. S. Hodges, J. Maze, M. D. Lukin, and P. Cappellaro, J. Chem. Phys. **133**, 124105 (2010).

METHODS

Measurement-based vs. coherent feedback

In feedback protocols, the goal is to control an open system (the plant) so that it undergoes a desired evolution or it reaches a desired state. To achieve this goal, feedback protocols engineer a second system (the controller) connected to the plant. In quantum feedback there are two possible strategies: in the first one, we measure the plant output and engineer a classical controller that manipulates the plant according to the measurement result (this is called a measurement-based feedback protocol). In the second strategy, the controller is a second quantum system, coherently coupled to the plant. This strategy, called *coherent feedback* [9], allows avoiding measurements. The controller can gain information about the plant state by coherent operations, sharing information about the state via entangling operations. Then, the controller can manipulate the plant based on this information to achieve the desired plant dynamics, by performing conditional operations on the plant.

While the first strategy is more intuitive and closer to the classical scenario, coherent feedback is more intriguing, both from a theoretical point of view, for its relation to information and entanglement theory, and from an experimental one, as avoiding measurements often simplifies the experimental implementation. We also note that coherent feedback formally encompasses measurement-based feedback and, as we did in this work, one can transform a measurement-based protocol into a coherent one. To clarify the two strategies, we present the feedback protocol we considered [16] using both strategies.

In both protocols, the ancillary qubit is first prepared in a superposition state, so that the initial state of the combined system is $|\Psi_0\rangle = \frac{1}{\sqrt{2}}(|0\rangle_a + |1\rangle_a)\,|\phi\rangle_q\,|\xi\rangle_b$, where $|\xi\rangle_b$ and $|\phi\rangle_q$ are the initial state of the bath and qubit, respectively. The qubit and the ancilla are then entangled by a controlled operation U_c, $|\Psi_1\rangle = \frac{1}{\sqrt{2}}(|0\rangle_a\,|\phi\rangle_q + |1\rangle_a\,U_c\,|\phi\rangle_q)\,|\xi\rangle_b$. The choice of U_c depends on the type of noise one wishes to refocus. As explained in details in Ref.[16], U_c can be chosen so that it transforms the qubit-bath interaction into a block-diagonal form. This in turns will allow to perform appropriate correction operations in each sub-manifold of the qubit. More intuitively, if the action of the bath can be represented by a random unitary operator $U_{qb} = e^{i\varphi_r \vec{\sigma}\cdot\vec{n}}$, with ϕ_r random and $\vec{n}$ a unit vector, U_c should invert the action of the bath, that is, $U_c^\dagger U_{qb} U_c = U_{qb}^\dagger$. After the system evolves under the action of the bath (and possibly of a desired gate) the entangling operation is undone, $|\Psi_2\rangle = \frac{1}{\sqrt{2}}(|0\rangle_a\,U_{qb}\,|\phi\rangle_q\,|\xi\rangle_b + |1\rangle_a\,U_c^\dagger U_{qb} U_c\,|\phi\rangle_q\,|\xi\rangle_b)$. Owing to the entanglement, information about the action of the bath is encoded in the state of the ancilla. Thus, in the measurement-based feedback algorithm, the ancilla state is measured (in the x-basis) and depending on the outcome

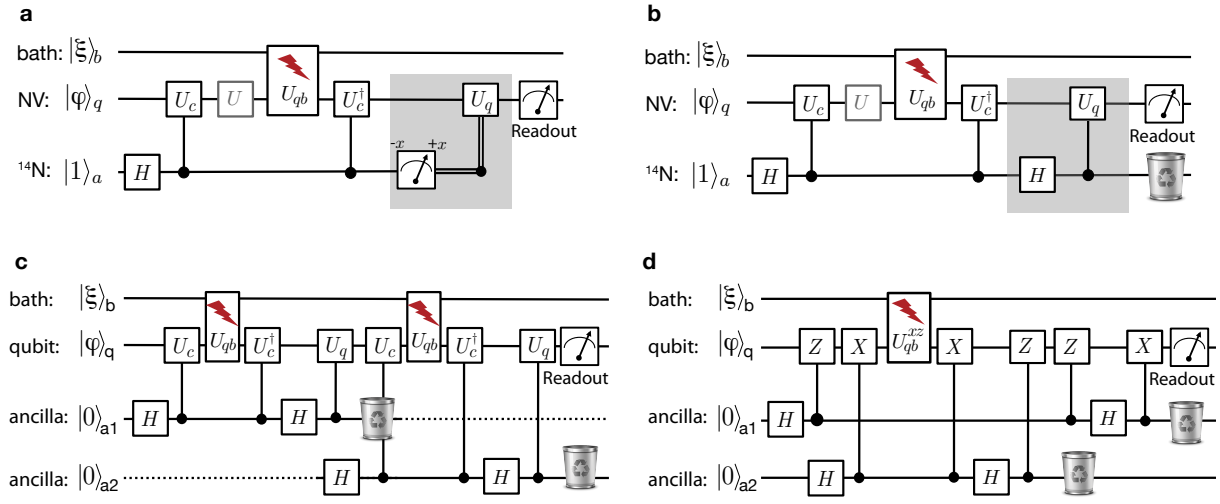

FIG. 1. **Feedback Circuit** (see e.g. [37] for explanation of the notations). **(a)** Measurement-based and **(b)** coherent feedback algorithms. In the shaded regions we highlight the differences between the two strategies. The measurement-based protocol requires a measurement of the ancilla and subsequence classically-controlled operation (double lines indicate a classically wire). The coherent feedback protocol instead does not perform a measurement but requires a coherent controlled operation. **(c)** Re-initializing the ancilla or using multiple fresh ancillas can extend the feedback protection beyond the ancilla's coherence time. **(d)** A concatenated feedback algorithm with two ancillas can protect the qubit from general noise (applied along any axis).

a classical control operation is applied to the qubit. Indeed we can rewrite the state just before the measurement as

$$|\Psi_2\rangle = \frac{1}{2}[|+\rangle (U_{qb} + U_c^\dagger U_{qb} U_c) + |-\rangle (U_{qb} - U_c^\dagger U_{qb} U_c)] |\phi\rangle_q |\xi\rangle_b ,$$

where $|\pm\rangle$ are eigenstates of σ_x^a. With an appropriate choice of U_c, $K^\pm = U_{qb} \pm U_c U_{qb} U_c^\dagger$ reduce to $K^+ = \mathbb{1}_q \otimes \chi_b^+$ and $K^- = U_q^\dagger \otimes \chi_b^-$, where $\chi_b^\pm$ are operators acting on the bath only and U_q is a unitary acting on the qubit. If the measurement of the ancilla yields the negative eigenstate, we then apply the correction operation U_q, which is a unitary that depends on the type of bath that affects the qubit. In the simple noise model we considered above (a unital noise with a stochastic Hamiltonian generator $H_r \propto \vec{\sigma} \cdot \vec{n}$), the correction operation is $U_q = i\vec{\sigma} \cdot \vec{n}$.

In the experimental implementation, the main source of decoherence is dephasing noise, thus we fixed $U_c = \sigma_x$ and $U_q = \sigma_z$. In a magnetometry scenario, when we want to correct for bit-flip errors while measuring longitudinal external fields, the gates would be $U_c = \sigma_z$ and $U_q = \sigma_x$.

In the coherent feedback strategy, the measurement and classical correction operation are replaced by a coherent conditional operation (see Extended Data Fig. 1.a-b). Indeed the measurement (that is, conveying information to an external observer) is not needed for the ancilla to be able to perform a correction operation, since the ancilla already encodes the necessary information about the qubit state and the action of the noise.

At the end of the feedback protocol, the ancilla can be recycled to perform a second round of protection, thus allowing to extend the protection beyond the ancilla's coherence time. In the current experiment, one could achieve the first strategy by using coherent polarization exchange between the NV and ^{14}N spins at lower (or much higher) magnetic field, where optical polarization leaves the nuclear spin untouched. After a first run of the algorithm (for a protection time $\tau < T_{2n}^\star$) one could swap the state of the NV electronic and nuclear spins, re-polarize the NV center and swap back the state from the nuclear spin to the NV, before applying the feedback protection for another stretch of time. Alternatively, if the ancilla cannot be re-initialized, one could use additional fresh ancillas (see Extended Data Fig. 1.c), for example other ^{13}C nuclear spins in the lattice. If two ancillas are available, one can construct a concatenated feedback algorithm (see Extended Data Fig. 1.d) that protects the qubit against multi-axis noise. The qubit is then protected against e.g. both dephasing (T_2) and depolarizing (T_1) noise. More broadly, the feedback protection algorithm could provide a first layer of protection against the strongest noise source, and be combined with more advanced quantum error-correcting codes (even on the ancilla itself) with the goal of achieving fault tolerance.

Modeling of the time evolution of the qubit-ancilla system

We study the time evolution of the qubit during the algorithm under the effects of a bath, to better understand the action of the feedback-based protection algorithm and obtain insight of its limits. While in the experiment noise emerges from a spin bath with non-Markovian character, we can employ a simpler model with a Markovian bath to find an analytical solution, since it yields the same result up to a different form of the exponential decays.

In the model, we consider dephasing of the qubit and ancilla, and the lattice relaxation of the qubit, characterized by the time scales $T_{2e}^\star$, $T_{2n}^\star$ and T_{1e} respectively. Letting ρ be a state of the qubit and the ancilla, the time evolution under the Markovian environment is determined by the Lindblad equation [31]:

$$\frac{d}{dt}\rho = i[\rho, \mathcal{H}] + \sum_k (L_k \rho L_k^\dagger - \frac{1}{2}\rho L_k^\dagger L_k - \frac{1}{2} L_k^\dagger L_k \rho), \tag{1}$$

where $L_1 = \sqrt{\frac{1}{2T_{2e}^\star}}\sigma_z^e$, $L_2 = \sqrt{\frac{1}{T_{1e}}}\sigma_+^e$, $L_3 = \sqrt{\frac{1}{T_{1e}}}\sigma_-^e$ and $L_4 = \sqrt{\frac{1}{2T_{2n}^\star}}\sigma_n^e$. Given an initial state $\rho_0 = |0\rangle\langle 0|_e \otimes |1\rangle\langle 1|_n$, the state after the NOOP gate for a protection time τ is given by

$$\begin{aligned}\rho(\tau) = \; & \tfrac{1}{4}\mathbb{1} - \tfrac{1}{4}e^{-\frac{\tau}{T_{1e}}}\cos^2(\tfrac{A\tau}{2})\left[e^{-(\frac{1}{4T_{2e}^\star}+\frac{1}{4T_{2n}^\star})\tau}\sigma_z^n + e^{-\frac{\tau}{4T_{2n}^\star}}\sigma_z^e + e^{-\frac{\tau}{4T_{2e}^\star}}\sigma_z^e\sigma_z^n\right] + \\ & \tfrac{1}{8}e^{-(\frac{1}{T_{1e}}+\frac{1}{4T_{2e}^\star}+\frac{1}{4T_{2n}^\star})\tau}\sin(A\tau)(\sigma_x^n - \sigma_x^e\sigma_x^n) + \tfrac{1}{8}e^{-(\frac{1}{T_{1e}}+\frac{1}{4T_{2e}^\star})\tau}\sin(A\tau)(-\sigma_y^e + \sigma_y^e\sigma_y^n) + \\ & \tfrac{1}{4}e^{-\frac{\tau}{T_{1e}}}\sin^2(\tfrac{A\tau}{2})\left[e^{-(\frac{1}{4T_{2e}^\star}+\frac{1}{4T_{2n}^\star})\tau}\sigma_x^e\sigma_z^n + e^{-\frac{\tau}{4T_{2n}^\star}}\sigma_z^e\sigma_y^n + e^{-\frac{\tau}{4T_{2e}^\star}}\sigma_y^e\sigma_x^n\right].\end{aligned} \tag{2}$$

The effectiveness of the feedback-based protection algorithm can be evaluated by measuring the probability of retaining the initial qubit state. The fidelity is then given by the ideal normalised measurement operator $\overline{M}_0 = |0\rangle\langle 0|_e$:

$$\overline{S}(\tau) = \mathrm{Tr}[\rho(\tau)\overline{M}_0] = \frac{1}{2} - \frac{1}{2}\cos^2\left(\frac{A\tau}{2}\right)\exp\left[-\left(\frac{\tau}{T_{1e}} + \frac{\tau}{4T_{2n}^\star}\right)\right]. \tag{3}$$

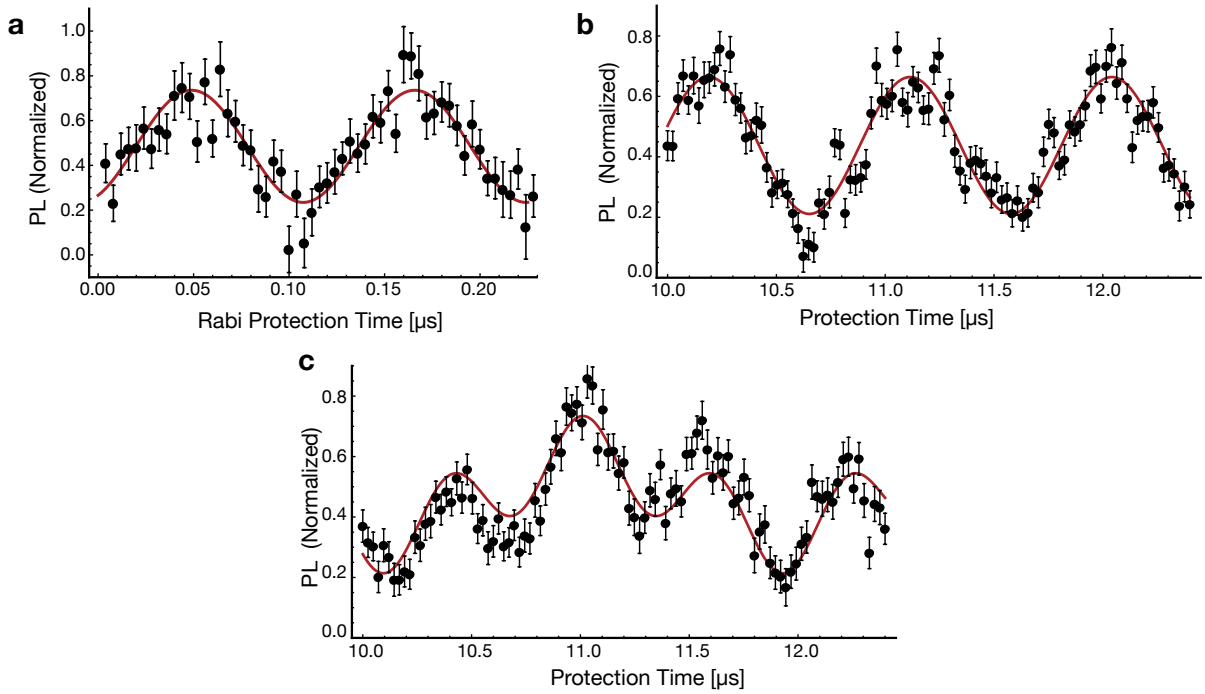

FIG. 2. **Protected Gate**: The feedback algorithm is compatible with application of NOT gates at any point during the protection time. **(a)** Rabi oscillations embedded in the feedback-based protection algorithm. **(b)** When the NOT gate is applied in the middle of the protection time, it reduces by half the period of oscillations due to the hyperfine coupling (See Eq. 5). **(c)** More complex evolution is obtained when inserting the NOT gate at other times. Here we show the behavior for $\tau_\pi = \tau/4$. Black dots are experimental data with error bars representing their standard deviation (see Fig. 2) and the solid lines are fittings to Eq. (5).

This result clearly indicates that the fidelity is not limited by the dephasing of the qubit $T^\star_{2e}$, but by that of the ancillary spin and the T_{1e} relaxation time of the qubit.

If instead we measure the normalised observable at the magnetic field corresponding to the excited state level anticrossing, we gather some information about the ancilla, resulting in a degradation of the protection:

$$\begin{aligned}\overline{S}(\tau) = \ & \mathrm{Tr}[\rho(\tau)\overline{M}] = \tfrac{1}{2} - \tfrac{1}{4}(\epsilon+\eta) - \tfrac{1}{2}e^{-(\frac{1}{T_{1e}}+\frac{1}{4T^\star_{2n}})\tau}\cos^2\left(\tfrac{A\tau}{2}\right) + \\ & \tfrac{1}{4}e^{-\frac{\tau}{T_{1e}}}\cos^2\left(\tfrac{A\tau}{2}\right)\left[(\epsilon-\eta)(e^{-\frac{\tau}{4T^\star_{2e}}}+e^{-\frac{\tau}{4T^\star_{2n}}}) - (\epsilon+\eta)e^{-(\frac{1}{4T^\star_{2e}}+\frac{1}{4T^\star_{2n}})\tau}\right]\end{aligned} \tag{4}$$

While the first line still indicates that the state is protected by the presence of the ancilla, terms in the second line, which decay at the rate of $T^\star_{2e}$, originate from the measurement of the ancilla spin and can be observed as a reduction of the oscillations of signal in the experiment.

In the main text we showed how it is possible to perform a NOT gate during the protection time. As the gate time is typically short (58ns in our experiments), we studied the subsequent evolution of the qubit, to show that its coherence is preserved for times longer than the dephasing time, $T^\star_{2e} \approx 4\mu s$. In addition, it is possible to insert the NOT gate at any point during the protected evolution. Due to the coupling with the ancilla qubit, the resulting signal is given by

$$\overline{S}_\pi(\tau,\tau_\pi) = \mathrm{Tr}[\rho_\pi(\tau,\tau_\pi)\overline{M}_0] = \frac{1}{2} + \frac{1}{4}[\cos(A\tau - A\tau_\pi) + \cos(A\tau_\pi)]\exp\left[-\left(\frac{\tau}{T_{1e}} + \frac{\tau}{4T^\star_{2n}}\right)\right], \tag{5}$$

where τ_π is the time at which the NOT gate is applied (with τ the total protection time). This expression was used to fit the experimental results obtained in the main paper and the data presented in Extended Data Fig. (2).

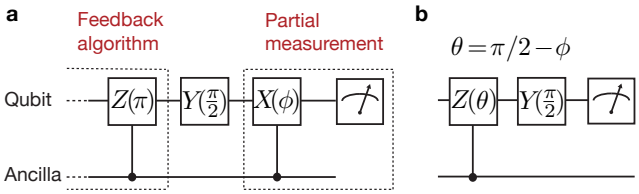

FIG. 3. **Weak measurement circuit.** (**a**) After the feedback algorithm is completed, a controlled-X rotation entangles the qubit with the ancilla, allowing us to perform a partial measurement of the ancilla: $|\psi\rangle_e(\alpha|1\rangle_n+\beta|0\rangle_n)\rightarrow\alpha\cos(\phi)|\psi\rangle_e|1\rangle_n+\beta\sin(\phi)(\sigma_x|\psi\rangle_e)|0\rangle_n$. The strength of the measurement can be adjusted by the angle ϕ. (**b**) The control sequence in (a) can be simplified by combining the partial measurement gates with the preceding gates of the feedback algorithm. As a result, to implement the weak correlated measurement in the experiment, we simply perform a controlled-phase rotation gate with $\theta=\pi/2-\phi$, instead of the controlled-Z ($\theta=\pi$) rotation required for the feedback algorithm.

Weak measurement of the ancilla-qubit correlation

In order to observe the compromise between protection and information gained on the ancillary qubit, we perform a weak measurement of the nuclear-electronic spin correlation, by applying a conditional gate after the feedback algorithm and prior to the detection of the NV electronic spin by optical readout. As shown in Fig. 3.(a), the weak measurement could be obtained by applying a conditional rotation of the NV electronic spin, after that spin has been rotated back to its population state by a $\pi/2$ pulse. The rotation angle ϕ determines the strength of the measurement.

These additional gates can however be avoided, by noting that the circuit is equivalent to replacing the conditional π Z-gate with a conditional θ Z-gate, where $\theta=\pi/2-\phi$ sets the measurement strength, see Fig.3-(b).
The state after the feedback algorithm is given by

$$\begin{aligned}\rho_\theta(\tau) &= \tfrac{1}{4}\mathbb{1}-\tfrac{1}{4}e^{-\frac{\tau}{T_{1e}}}\cos^2(\tfrac{A\tau}{2})\left[e^{-(\frac{1}{4T_{2e}^\star}+\frac{1}{4T_{2n}^\star})\tau}\sigma_z^n+e^{-\frac{\tau}{4T_{2n}^\star}}\sigma_z^e+e^{-\frac{\tau}{4T_{2e}^\star}}\sigma_z^e\sigma_z^n\right]+\\ &\tfrac{1}{8}e^{-\frac{\tau}{T_{1e}}}(e^{-\frac{\tau}{T_{2n}^\star}}-e^{-\frac{\tau}{T_{2e}^\star}})\cos^2(\tfrac{A\tau}{2})\alpha(\theta)(\sigma_z^e+\sigma_z^e\sigma_z^n)+...\end{aligned} \tag{6}$$

where $\alpha(\theta)=1+\frac{\cos(A\tau/2+\theta)}{\cos(A\tau/2)}$. Assuming no contrast of the measurement of the nuclear spin ($\epsilon=\eta=0$), the signal is then given by

$$\overline{S}_\theta(\tau)=\frac{1}{2}-\frac{1}{2}e^{-(\frac{1}{T_{1e}^\star}+\frac{1}{4T_{2n}^\star})\tau}\cos^2\left(\frac{A\tau}{2}\right)+\frac{1}{2}e^{-\frac{\tau}{T_{1e}}}(e^{-\frac{\tau}{T_{2n}^\star}}-e^{-\frac{\tau}{T_{2e}^\star}})\cos^2\left(\frac{A\tau}{2}\right)\alpha(\theta). \tag{7}$$

While for $\theta=\pi$ ($\alpha=0$) we recover the ideal fidelity, protected against the electron dephasing noise, when $\theta\neq\pi$ we perform a partial measurement of the ancilla, but the signal now decays at the time constant $T_{2e}^\star$.

Experimental setup

Experiments were performed using an electronic grade single crystal diamond plate provided by Element 6, with [100] orientation and a nominal nitrogen concentration less than 5 ppb. A home-built confocal microscope was used to scan the sample (scanning piezo stage Nano-3D200, Mad City Labs) and measure a single naturally occurring Nitrogen Vacancy (NV) centre situated $\sim 10\mu$m from the surface of the diamond. The NV centre is coherently excited by a optical pulse at 532 nm provided by a diode-pump laser (Coherent Compass 315M) and shaped by a acoustic optical modulator (AOM) with rise time $\leq$ 7ns (1250C-848, Isomet), and then delivered by means of a 100x, NA = 1.3 oil immersion objective lens (Nikon Plan Fluor). The fluorescence by the NV centre is collected by the same objective lens and then sent to a single-mode broadband fiber of NA = 0.12 (Font Canada), being connected to a single photon detector (SPCM-AQRH-13-FC, Perkin Elmer). An Arbitrary Waveform Generator (AWG) with 1.2 GS/s (AWG5014B, Tektronix) plays a central role in generating microwave (MW) pulses and radio frequency (RF) pulses, as well as timing the AOM and the single photon detector. MW pulses are shaped by mixing the signal from the AWG with a carrier MW field provided by a signal generator (N5183A-520, Agilent) with the aid of an I/Q mixer (IQ-0318L, Marki Microwave) and then cleaned up by a switch (ZASWA-2-50DR+, Mini-Circuits) while RF pulses are directly generated by the AWG. The MW pulse and RF pulses are combined after amplification (GT-1000A, Gigatronics for MW and LZY-22+, Mini-Circuits for RF) and delivered to the sample via a thin copper wire with a diameter of 25 μs (Alfa Aesar).

Dynamics and control of the two-qubit system

1. Hamiltonian of the NV-^{14}N system

The NV centre spin system consists of the electronic spin ($S = 1$) and the nitrogen nuclear spin ($I = 1$) that interact strongly via the hyperfine coupling ($A \approx -2.15$ MHz). A static magnetic field is applied to lift the degeneracy of the electronic $m_s = \pm 1$ and nuclear spin $m_I = \pm 1$ levels, thus yielding the Hamiltonian

$$\mathcal{H} = \Delta S_z^2 + \omega_e S_z + Q I_z^2 + \omega_n I_z + A S_z I_z, \tag{8}$$

where S and I are the electron and nuclear spin operator respectively, $\Delta = 2.87$ GHz is the electronic zero-field splitting and $Q = -4.95$ MHz the nuclear quadrupolar interaction.

We define one qubit in the electronic spin subspace as $|m_s = 0\rangle \equiv |1\rangle_q$ and $|m_s = -1\rangle \equiv |0\rangle_q$. A second, ancillary qubit is defined in the subspace of the nuclear spin as $|m_I = +1\rangle \equiv |1\rangle_a$ and $|m_I = 0\rangle \equiv |0\rangle_a$. Both spins are driven on-resonance on these selected transitions; we can thus neglect other parts of the Hilbert space and only express the Hamiltonian in the rotating frame in the subspace of interest. We then rewrite the Hamiltonian in terms of spin-1/2 operators $\sigma^{e,n}_{x,y,z}$ defined by the basis above as follows,

$$\mathcal{H} = \frac{A}{4}(-\sigma_z^e + \sigma_z^n - \sigma_z^e \sigma_z^n). \tag{9}$$

The hyperfine interaction induces a frequency shift, thus enabling to adjust the selectivity of the MW pulse by tuning the transition rate (Ω_e). A strong driving, $\Omega_e = 20$MHz $\gg A$, is employed to drive the qubit non-selectively for any ancilla state, while $\Omega_e = 500$kHz $\ll A$ is used to drive the qubit selectively on the ancilla state, thus engineering conditional gates. The RF frequency is on resonance with the transition between $|0,1\rangle$ and $|0,0\rangle$. The transition rate is around $\Omega_n = 20 - 40$ kHz, which already reflects an enhancement due to electronic virtual transitions mediated by the transverse component of the hyperfine coupling [21]. Since the nuclear Rabi transition rate is always smaller than the detuning given by the hyperfine interaction ($\Omega_n \ll A$), only selective driving of the ancillary spin is available and unconditional gates need to be engineered with composite pulses.

2. Coherent control of the nuclear spin

The ^{14}N nuclear spin is coherently controlled by employing a resonant RF field. In general, the nuclear spin state cannot be directly measured optically with high fidelity. Thus, after driving the nuclear spin, we apply a gate to map the nuclear spin state to the NV electronic spin [Fig.4-(a)]. In order to calibrate quantum gates required for the feedback-based protection algorithm ($\pi/2$-rotation), we first characterize the nuclear spin, by measuring the resonance frequency of the transition $|1\rangle_q |1\rangle_a \leftrightarrow |1\rangle_q |0\rangle_a$ [Fig.4-(b)] and the nuclear Rabi oscillations [Fig.4-(c)]. We note that despite the small gyromagnetic ratio of the nitrogen ($\gamma_n = 0.308$ kHz/G) its Rabi oscillations are significantly enhanced due to the transverse hyperfine coupling with the NV spin (we achieve an enhancement factor of about 20 over the bare Rabi frequency around 500 G [21]). To further characterize the nuclear spin ancillary qubit, we measured the dephasing time, $T_{2n}^\star$, by performing a Ramey experiment [Fig.4-(d] and obtained $T_{2n}^\star \approx 3.2$ ms.

While the dynamics of the ^{14}N spin under RF driving is relatively simple when the NV electronic spin is in one of the population states, further complications arise when the NV qubit is in a superposition state, that stem from the electronic spin decoherence, its evolution due to the RF driving, and due to the hyperfine interaction.

For a typical nuclear spin gate, such as the $\pi/2$ rotation required for the algorithm, we need to consider decoherence process of the electronic spin, which progresses at a faster rate ($T_{2e}^\star \sim 4\mu$s) than the gate operation ($t_\pi \sim 30\mu$s). In addition, we need to engineer unconditional gates, even when the driving field can only rotate the nuclear spin in one of the electronic spin manifolds. In order to protect the qubit state during the gate operation, a MW π pulse is inserted in the middle of the RF pulse and is then compensated by adding a second MW -π pulse at the end of the RF pulse. This procedure simultaneously also solves the second issue, as it produces a non-selective gate. The Hamiltonian under the RF driving in the rotating frame is given by $\mathcal{H} = \mathcal{H} + \mathcal{H}_{\rm RF}$ with

$$\mathcal{H}_{\rm RF}(t) = -\frac{1}{2}\Omega_e \sigma_z^e \cos(\omega_{\rm RF} t + \phi) + \sqrt{2}\Omega_n \sigma_x^n. \tag{10}$$

Here $\Omega_{e,z}$ and Ω_n are the coupling strength of the electronic spin and the nuclear spin with the longitudinal and transverse component of the RF field respectively. We can neglect the coupling of the nuclear spin with the longitudinal component of the RF field as well as the transverse component of the RF effects on the electronic field, since at most

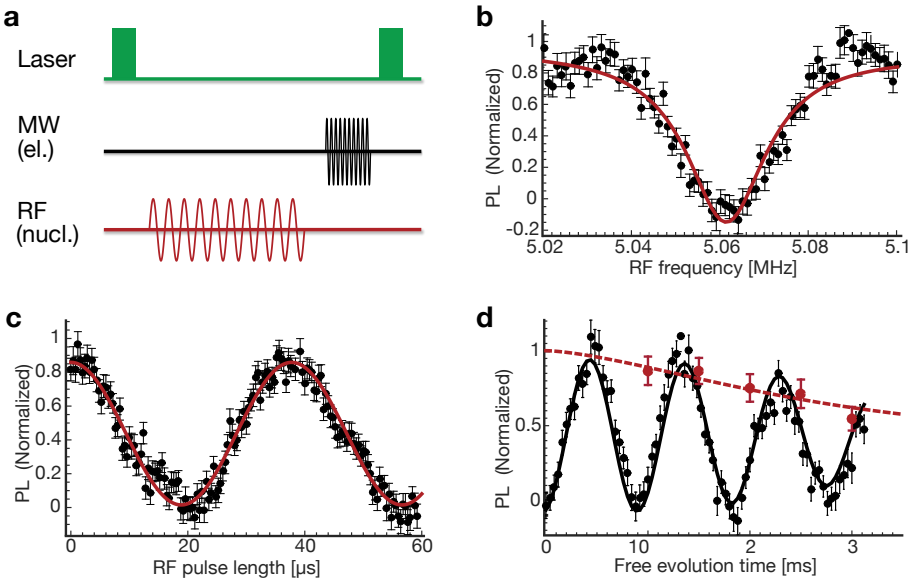

FIG. 4. **Control and coherence of the nitrogen nuclear spin.** **(a)** *Typical control sequence*: The first laser pulse initialises the spins into the $|0,1\rangle$ state. After a nuclear spin gate (RF driving), to detect the nuclear spin state we employ a MW selective π-pulse that maps the nuclear spin state onto that of the NV spin, which is subsequently detected by the second laser pulse. **(b)** *Nuclear magnetic resonance at* $\sim$ 390 G. We sweep the RF frequency at fixed pulse length. The spectrum dip indicates the resonant frequency of the $|0,1\rangle \leftrightarrow |0,0\rangle$ transition. **(c)** *Nuclear Rabi oscillations.* We drive resonantly the $|0,1\rangle \leftrightarrow |0,0\rangle$ transition. The measured nutation rate (Rabi frequency) is $\Omega_n \approx 26.3$ kHz [21]. **(d)** *Nuclear Ramsey fringes* under the sequence $\pi/2-\tau-\pi/2$, where τ is the free evolution time. We measure a dephasing time of the nuclear spin $T_{2n}^{\star} = 3.2$ ms, which is limited by the NV electronic spin lattice relaxation process ($T_1 = 4.5$ ms, red circles and dashed line). Error bars in (c-d) represent the signal standard deviation, calculated by error propagation from the PL intensity of the signal and reference PL curves acquired for each data point for $m_s = \{0,-1\}$.

it induces a resonance shift (Bloch-Siegert shift [32]) that is however refocused by the MW π pulses embedded in the RF pulse. The longitudinal driving imposes an additional, quite large, phase modulation $\Theta(\tau)$ on the NV spin, even in the presence of the spin echo π pulses:

$$\Theta(\tau) = -\frac{\Omega_e}{4}\Big(\int_0^{\tau}\cos(\omega_{\rm RF}t+\phi)dt + \int_{\tau}^{2\tau}\cos(\omega_{\rm RF}t+\phi)dt\Big) = \frac{2\Omega_e}{\omega_{\rm RF}}\cos(\omega_{\rm RF}\tau+\phi)\sin(\frac{\omega_{\rm RF}\tau}{2})^2. \tag{11}$$

While in principle one can remove this phase by a proper selection of the timing, in practice this often clashes with other time requirements set by the need to refocus effects due to the hyperfine couplings (explained below).

In our experiment, we used a more flexible strategy to remove this undesired modulation, by employing time-proportional phase incrementation [33] (TPPI) of the RF phase $\phi(\tau)$. $\Theta(\tau)$ in Eq. 11 can indeed be canceled at any time by selecting $\phi(\tau) = -\omega_{RF}\tau$. Unlike stroboscopic detection with time interval $\delta\tau = 2\pi/\omega_{\rm RF}$, TPPI enables continuous measurement of the ^{14}N spin Rabi driving and it is also of great use when the time resolution of experiment system is limited and one cannot select $\delta\tau$ with enough precision. Defining $U(\tau) = \exp(-i\mathcal{H}\tau)$ and $R_{\pm\pi} = \exp(\mp i\pi\sigma_x^e)$, the two-spin propagator $V(\tau)$ under TPPI conditions is given by

$$\begin{aligned} V(\tau) &= R_{-\pi}U(\tau)R_{\pi}U(\tau) = e^{-i\left[\frac{A}{4}(\sigma_z^e+\sigma_z^n+\sigma_z^e\sigma_z^n)+\sqrt{2}\Omega_n\sigma_x^n\right]\tau}e^{-i\left[\frac{A}{4}(-\sigma_z^e+\sigma_z^n-\sigma_z^e\sigma_z^n)+\sqrt{2}\Omega_n\sigma_x^n\right]\tau} \\ &= \cos\left(\sqrt{2}\Omega_n\tau\right)\left[\cos\left(\tfrac{At}{2}\right)\mathbb{1} - i\sin\left(\tfrac{At}{2}\right)\sigma_z^n\right] - i\sin\left(\sqrt{2}\Omega_n\tau\right)\left[\cos\left(\tfrac{At}{2}\right)\sigma_x^n + \sin\left(\tfrac{At}{2}\right)\sigma_z^e\sigma_x^n\right], \end{aligned} \tag{12}$$

where we took the limit $A \gg \Omega_n$ to neglect off-resonance driving. We note that due to the combination of the hyperfine coupling $A\sigma_z^e\sigma_z^n/4$ and the RF driving $\frac{1}{2}\Omega_n B_{1x}\sigma_x^n$, the propagators of the nuclear spin before and after the MW π pulse do not commute and the nuclear spin evolves about non-parallel axes in the two time intervals. This can be directly observed as a modulation of the electronic spin echo, similar to the more common ESEEM [34] for anisotropic hyperfine coupling. In order to avoid the effects of the hyperfine, we can set $A\tau = 2\pi$. Since $A \gg \Omega_n$, we can choose a timing τ fulfilling both the above condition and the desired RF pulse time, yielding $V(\tau) = \sigma_x^n$.

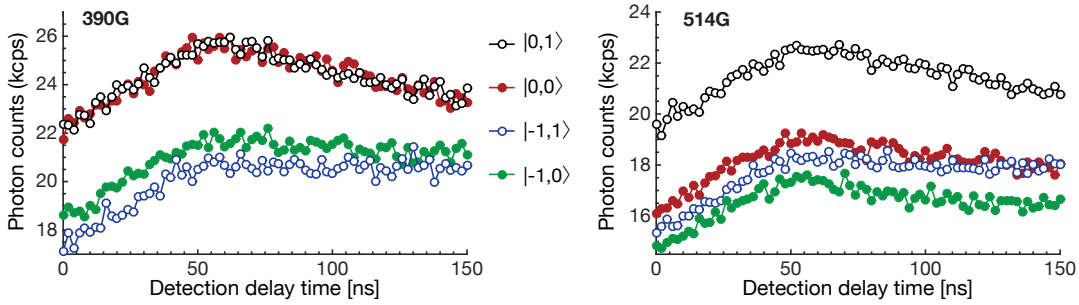

FIG. 5. **Electronic and nuclear-spin dependent fluorescence at different magnetic field strengths.** At the lower magnetic field (left, B= 390G), the fluorescence intensity shows only a weak dependence on the nuclear spin state in the $m_s = -1$ manifold, whereas at B=514 G, which is very close to the ESLAC, a strong dependence on the nuclear spin state is observed in both manifolds (right panel). From these fluorescence measurements, we obtained the parameters (ϵ, η) used to model the measurement operator. In the experiments, the detection time delay and window were optimised to obtain the maximum contrast of the state at each magnetic field.

3. Measurement model and nuclear-spin dependent fluorescence intensity

Measurement of the NV spin state is achieved by monitoring the photoluminescence (PL) under laser excitation at 532 nm. Thanks to spin-dependent photodynamics in the excited state, the PL intensity is correlated with the NV electronic spin population. In an addition, at magnetic fields close to the excited state level anticrossing (ESLAC), the PL intensity becomes modulated by the nuclear spin state as well, due to the strong hyperfine coupling between the electronic and the nuclear spins in the excited state [15, 35]. Thus the observable in the experiment can be modelled by the operator:

$$M = n_{1,1}\left|1,1\right\rangle\left\langle 1,1\right| + n_{1,0}\left|1,0\right\rangle\left\langle 1,0\right| + n_{0,1}\left|0,1\right\rangle\left\langle 0,1\right| + n_{0,0}\left|0,0\right\rangle\left\langle 0,0\right|, \tag{13}$$

where n_{m_q,m_a} are stochastic variables denoting the total number of photons [36] detected during the measurement time (300 ns) from the state being initially $|m_q, m_a\rangle$. In writing the observable, we neglected the $m_s = +1$ and $m_I = +1$ states, which are never populated in the experiment. In order to reduce the photon shot noise, all measurements are repeated 5×10^5 times. The raw PL signal S at each measured point of the sequence is normalised by the PL collected from two fiducial states $|1,1\rangle$ and $|0,1\rangle$. These states are prepared at each average from optical polarisation and optical polarisation followed by adiabatic passage of the electronic spin to the $|1,1\rangle$ state. The raw signal from a state ρ, is then normalised to yield

$$\overline{S} = \frac{\mathrm{Tr}\left\{M\rho\right\} - \langle n_{0,1}\rangle}{\langle n_{1,1}\rangle - \langle n_{0,1}\rangle} = \mathrm{Tr}\left\{\overline{M}\rho\right\}, \tag{14}$$

where we define the normalised measurement operator $\overline{M}$:

$$\overline{M} = \begin{bmatrix} 1 & 0 & 0 & 0 \\ 0 & 1-\epsilon & 0 & 0 \\ 0 & 0 & 0 & 0 \\ 0 & 0 & 0 & -\eta \end{bmatrix} = \frac{1}{4}\left[(2-\eta-\epsilon)\mathbb{1} + (\epsilon+\eta)\sigma_z^n + (\eta-\epsilon+2)\sigma_z^e + (\epsilon-\eta)\sigma_z^e\sigma_z^n\right]. \tag{15}$$

Here $\epsilon = (\langle n_{1,1}\rangle - \langle n_{1,0}\rangle)/(\langle n_{1,1}\rangle - \langle n_{0,1}\rangle)$ and $\eta = (\langle n_{0,1}\rangle - \langle n_{0,0}\rangle)/(\langle n_{1,1}\rangle - \langle n_{0,1}\rangle)$ describe the optical distinguishability of the nuclear spin states in each electronic manifold. Usually, the nuclear spin state does not affect PL intensity, i.e., $\epsilon = \eta = 0$, since it does not affect the relaxation process of the NV center. However, close to the ESLAC, dynamics driven by the strong excited-state hyperfine coupling renders the relaxation process of the NV spin correlated with the nuclear spin state [26], leading to a optical contrast among the nuclear spin states. Thus, the strength of measurement of the nuclear spin can be varied by changing the static magnetic field. In our experiments we choose two working conditions that, while still allowing nuclear spin polarisation ($P > 0.9$) by optical pumping, could highlight differences due to partial measurement of the ancilla spin. We thus performed the experiment at two different magnetic field (390G and 514 G) characterised by different strengths of the nuclear spin optical contrast ($\epsilon = 0.14$, $\eta = 0.16$ at $B = 390$G and $\epsilon = 0.86$, $\eta = 0.25$, for $B = 514$G). These values were estimated by measuring

the PL intensity for all four states (see Fig. 5).

[31] G. Lindblad, " On the generators of quantum dynamical semigroups," Communications in Mathematical Physics **48**, 119–130 (1976) .
[32] F. Bloch, " Generalized theory of relaxation," Phys. Rev. **105**, 1206 (1957) .
[33] M. Kälin and A. Schweiger, " Radio-frequency-driven electron spin echo envelope modulation spectroscopy on spin systems with isotropic hyperfine interactions," **115**, 10863–10875 (2001) .
[34] W. B. Mims, " Envelope modulation in spin-echo experiments," Phys. Rev. B **5**, 2409–2419 (1972) .
[35] P Neumann, R Kolesov, V Jacques, J Beck, J Tisler, A Batalov, L Rogers, N B Manson, G Balasubramanian, F Jelezko, and J Wrachtrup, " Excited-state spectroscopy of single nv defects in diamond using optically detected magnetic resonance," New J. Phys. **11**, 013017 (2009) .
[36] C. A. Meriles, L. Jiang, G. Goldstein, J. S. Hodges, J. Maze, M. D. Lukin, and P. Cappellaro, " Imaging mesoscopic nuclear spin noise with a diamond magnetometer," **133**, 124105 (2010) .
[37] M. A. Nielsen and I. L. Chuang, *Quantum computation and quantum information* (Cambridge University Press, Cambridge; New York, 2000) .